Journal of Applied Physics

AIP Publishing

Self-consistent statistical model for current transport in polycrystalline semiconductors

Eva L. C. Benford[1] and Iddo Amit[1]

Department of Engineering, Durham University, Stockton Road, Durham DH1 3LE, United Kingdom

(*iddo.amit@durham.ac.uk)

(Dated: 5 September 2024)

Transport in novel materials, specifically those scaled up to wafer sizes, will be dominated by thermionic emission over charged, randomly oriented grain boundaries. However, the challenges presented by random dopant fluctuation in lightly and moderately doped nanocrystalline materials are yet to be addressed. Here, we present a self-consistent model to describe the transport in polycrystalline materials with medium doping levels, where conductivity is governed by thermionic emission over low and wide barriers. We show that random doping fluctuations contribute to a higher material resistivity which is explained through a non-linear potential drop over the depletion regions on both sides of the boundary. This leads to a decrease in the exponential slope at the onset of conductivity, down to values of $\sim \exp(-2.4kT)^{-1}$, as well as to asymmetry in the current-voltage characteristics. We demonstrate that the model can be scaled up to several grains and their boundaries, by using commercially available circuit simulators, where non-linearity is realized through look-up tables. We find that an increase in resistivity of up to 18% compared to the nominal, uniformly doped material, can be explained simply by the introduction of random dopant fluctuations.

I. INTRODUCTION

Transport in polycrystalline semiconductors is attracting wide interest as new materials systems, such as van der Waals semiconductors[1] and transparent conductive oxides,[2] show great potential for the realization of two-dimensional electronic devices,[3] and photovoltaics,[2] as well as in more conventional devices.[4,5] Delivering on that promise can only be realized using wafer-scale growth and processing, which inevitably results in polycrystalline films[3,6] where transport properties are significantly different from the monocrystalline bulk.

The accepted theory of transport and electrostatics in polycrystalline media is underpinned by models introduced in the seminal works of Seto,[7] and Martinez and Piqueras,[8] following earlier observations on the mobility in polycrystalline silicon[9]. In short, the formation of defect-rich grain boundaries[10] results in the immobilization of free charge carriers between the grains and a decrease in the number of free carriers that can exceed 10^7 orders of magnitude compared to the nominal doping levels for realistic dispersion of interface state energies.[11] The build-up of a surface charge density depletes the grains, either wholly or partially, causing a potential barrier for transport between them. The potential barrier is a function of the doping levels, N_D, the grain length in the dimension normal to the boundary, L, and the density of trapping states, N_T. For cuboid grains, the potential barrier will increase with doping up to a limit where $N_D = N_T/L$, under which the grains are fully depleted, and then decrease as quasi-neutral regions begin to develop within the grains.[7] For spherical grains, $N_D = 3N_T/R_c$ where R_c is the critical radius.[12]

These considerations lead to an analytical electrostatic description of a typical grain, which is generalized to a bulk, but are based on a uniform distribution of doping and grain sizes throughout the material.[13] However, the random nature of crystal formation[14] as well as random dopant fluctuations[15] are inherent to the materials growth process, and contribute to a non-negligible random distribution of the density of free carriers within grains in materials with medium level doping and nanometre-size grains.

Random distribution of doping and grain sizes significantly impacts transport characteristics in polycrystalline thin film applications such as thin-film transistors (TFTs), as evidenced by the efforts to derive expressions for the threshold voltage[16] and field-effect mobility[17] in silicon TFTs. However to date, most approaches that address the challenges of incorporating an ensemble of grains into an analytical expression either assume similar potential barriers at grain boundaries[18,19], which is inconsistent with random doping fluctuations, or treat polycrystalline

transport using percolation theory[20], which neglects contribution from less conducting paths and cross-talk between paths.

Arguably the most significant factor in developing an accurate understanding of transport through grain boundaries is the division of potential drop between the two sides of the grain boundary. When the two depletion regions on both sides of the barrier are placed under bias, one contracts and its resistivity is reduced as if under forward bias conditions due to the injection of charges of similar polarity. The other extends due to the injection of opposite polarity charges and its resistivity increases. Despite the two sides of the boundary acting as a non-linear voltage divider, previous models assumed an equal potential drop over both sides of the barrier, which has been shown to be inconsistent with charge neutrality requirements[21]. However, the model suggested in [[21]] requires knowledge of the current, rendering it incompatible with simulations where multiple dissimilar boundaries are considered.

Here we develop a general self-consistent statistical model of the electrostatic structure and transport properties through grain boundaries with dissimilar doping. The model supports local variations in the density of free charges, consistent with a uniform random distribution of doping atoms under the assumption of established equilibrium, *e.g.*, that charge trapping has taken place. The presented model is valid for a wide range of doping densities, however, our focus here is on low- to medium-doping where charge redistribution through diffusion is hindered by the energy barriers at the grain boundaries.

The model is then scaled up to one-dimensional chains and two-dimensional networks, using large area circuit simulation methodology that has been demonstrated before for random RC networks[22] and porous conductors[23]. The material is 'reconstructed' in *LTspice*, a commercial circuit simulator by *Analog Devices*, with linear resistors emulating regions of the materials away from the grain boundaries, whereas grain boundaries and the quasi-neutral grains in their immediate vicinity are modelled as non-linear resistors using look-up tables constructed from the proposed model. We demonstrate that the transport properties in realistic polycrystalline materials can be accurately represented by a Weibull distribution which scales with the number of grains and grain boundaries in the system.

II. SELF-CONSISTENT MODEL OF POLYCRYSTALLINE TRANSPORT

A. Statistics of Charge Distribution.

When considering moderately doped nanocrystalline films, care must be given to the statistical distribution of dopant atoms per grain associated with low to medium level doping. For doping levels of 10^{15} or 10^{16} cm^{-3}, the mean distance between atoms is in the order of 125 and 60 nm, respectively. This implies that a spherical nano-crystallite with a radius of 100 nm and nominal doping levels of 10^{15} or 10^{16} cm^{-3} should contain on average four and 42 doping atoms, respectively. Thus, fluctuations of a few single atoms have large implications on the inter-crystallite doping levels.

It is important to highlight here the fundamental difference between chemical doping concentration, *i.e.*, the density of doping atoms in lattice sites, and the resulting density of free charge carriers in polycrystalline materials. For doping levels below 10^{19} cm^{-3}, the density of free charge carriers is many orders of magnitude below the chemical doping concentration, due to significant levels of charge trapping in interface states at the grain boundaries, and changes in a non-linear fashion as was shown *e.g.*, in [7]. This is a well understood phenomenon which is not critical for the model presented here. Therefore our focus will be on the effective carrier density, n_D, which is lower, possibly by a significant margin, from the chemical doping levels, N_D.

For a monocrystalline as well as highly doped polycrystalline systems, and in the absence of external excitation, localized variations such as these are insignificant, as the charge carriers rearrange through local diffusion to reach uniform distribution. However, in low- to medium-doped polycrystalline materials, where diffusion is hindered by the potential barriers at grain boundaries, variations in distribution remain localized, and as will be shown here, affect the conductance characteristics of the film.

To better understand the expected distribution of carrier densities, a cuboid bulk of material with a side length of 10 μm is simulated where 10^7 point-carriers are uniformly distributed, representing an effective density of 10^{16} cm^{-3}. Crucially, this distribution represents not only the initial arrangement of charge density, but is valid for any subsequent redistribution of charges following excitation where non-zero current is passed through the system, and the resulting distribution is non-uniform due to the obstructions for diffusion posed by the potential barriers at the grain boundaries. This charge density was chosen as it is in agreement with the assumptions dis-

cussed in the next section, namely, that grains with radii ranging between one hundred and a few hundreds of nanometers will not be fully depleted. The bulk cuboid is then sampled 8,000 times by choosing random points within the bulk, which are at least 500 nm from its edge, and counting the number of point carriers within a radius r_g ranging between 100 and 500 nm. A histogram of the results of the simulation with $r_g = 300$ nm is shown in Fig. 1 (a).

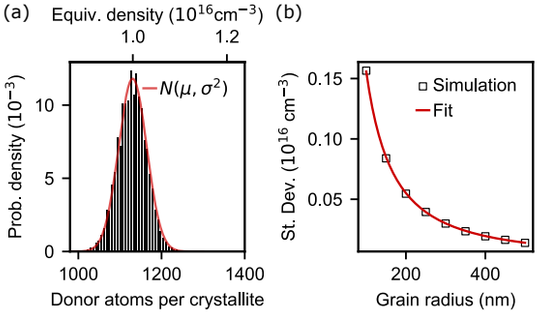

FIG. 1. (a) Distribution of the number of doping 'atoms' in a spherical grain with a radius of $r_g = 300$ nm. The population number is 8,000, and the solid red line shows a fit to normal distribution. (b) The standard deviation as a function of grain size. The solid red line shows a fit to $r_g^{-3/2}$.

The histogram displayed here fits a normal distribution with a mean value of 1130.6 and a standard deviation of 33.8 atoms per sphere which translate to mean effective density of $\mu_s = 1.00 \times 10^{16}$ and standard deviation of $\sigma_s = 0.03 \times 10^{16}$ cm^{-3} when normalized to the grain volume $v_g = (4/3)\pi \times r_g^3$. A Kolmogorov-Smirnov goodness of fit test confirmed the fit of the data to the distribution with a P-value of 0.1983 which is significantly larger than the critical value of 0.0182 for 0.01 significance level.

The results for $100 \geq r_g \geq 500$ nm[24–26] follow a similar pattern with a normalized mean effective density of 1.00×10^{16} cm^{-3} and a normalized standard deviation that decreases like a square root of the grain volume or $\sigma_s \propto r_g^{-3/2}$. The standard deviation values for grain sizes ranging from $100 \leq r_g \leq 500$ nm are displayed in Fig. 1 (b), along with their fit. These results will be utilized in the subsequent treatment of systems that consist of multiple grains.

B. Electrostatic of the Boundary of Dissimilar Grains.

The electrostatic model of a grain boundary and its depletion regions on both sides follows the same considerations used in Refs. [7,8]. The underlying assumptions are that (1) the depletion

approximation is a good description of the grain, *i.e.*, the grain is completely depleted within the depletion width x_i, where $i = 1$ or 2 are the two grains that form the boundary; (2) that the surface density of trapped charges n_T is constant, due to the small potential drop over individual grains and under steady-state conditions when transient process have ended; and (3) that the grain is not fully depleted, *i.e.*, that the effective doping $n_{D,i}$ satisfies $n_{D,i} > n_T/L$ where L is the grain length.

These assumptions translate to a space charge distribution across a two-grains 1-boundary (2G:1B) system given by $\rho_i = qn_{D,i}$, within the i^{th} side depletion region, and zero outside of it. Charge neutrality requires that the sum of depletion charges on both sides of the grain boundary balance the trapped surface charge at the boundary:

$$x_1 n_{D,1} + x_2 n_{D,2} = n_T \tag{1}$$

Solving the Poisson equation for the two depletion regions yields expressions for potential across the boundary region:

$$\psi_1 = \frac{qn_{D,1}(x+x_1)^2}{2\varepsilon} + K_1 \tag{2a}$$

$$\psi_2 = \frac{qn_{D,2}(x-x_2)^2}{2\varepsilon} + K_2 \tag{2b}$$

Where K_1 and K_2 are reference levels that depend on the boundary conditions. If ψ_i is chosen to describe the conduction band potential, it can be shown that its value at the left edge ($i = 1$) of the depletion region is $\psi_1(-x_1) = kT\ln(N_C/n_{D,1})$, where k is the Boltzmann constant, T the absolute temperature, and N_C is the effective density of states in the conduction band. Similarly, the potential on the right edge of the depletion region is $\psi_2(x_2) = kT\ln(N_C/n_{D,2}) - V_A$, where an arbitrary external bias V_A has been added as a boundary condition, such that the application of positive bias lowers the potential of the conduction band on the right hand side.

The requirement for potential continuity at the boundary ($x = 0$) provides the second equation required to determine the location of the depletion edges.

$$\frac{qn_{D,1}x_1^2}{2\varepsilon} = \frac{qn_{D,2}x_2^2}{2\varepsilon} + kT\ln\left(\frac{n_{D,1}}{n_{D,2}}\right) - V_A \tag{3}$$

Where the logarithm terms have been grouped on one side for simplicity.

Solving Eqs. 1 and 3 allows the determination of the depletion widths, x_1 and x_2. When $V_A = 0$, the solution yields the equilibrium depletion width, from which both built-in potentials, $V_{bi}^{(1)}$ and $V_{bi}^{(2)}$ can be evaluated using:

$$V_{bi}^{(1)} = \frac{qn_{D,1}x_1^2}{2\varepsilon} \tag{4a}$$

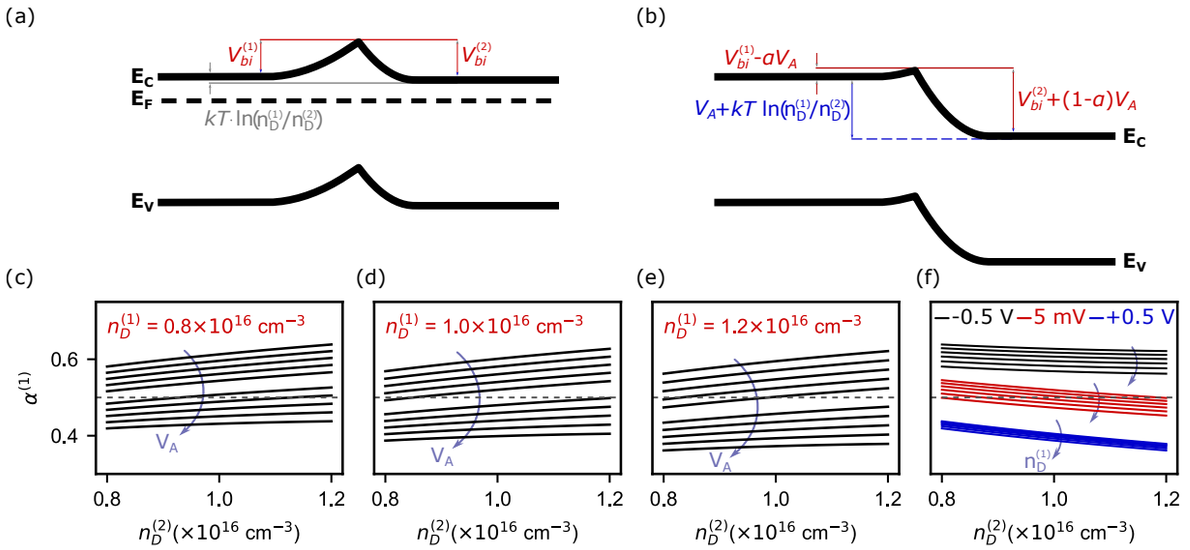

FIG. 2. (a)+(b) Band structure of a grain boundary and its immediate vicinity, for a dissimilar charge density profile where $n_{D,1} < n_{D,2}$. The bands are shown in equilibrium conditions (a) and under bias (b). (c)-(e) Values of the potential drop fraction, α as a function of RHS charge density levels for varying levels of LHS charge density (indicated on each panel) and applied external bias. The bias increases monotonously from -0.5 to $+0.5$ V from the top to the bottom, as indicated by the arrow. The line for $V_A = 0$ V is not shown as α is not defined for zero bias. (f) Values of α as a function of RHS charge density for different levels of applied bias, indicated on the panel, and LHS charge density monotonously varying from 0.8 to 1.2×10^{16} cm^{-3} in the direction indicated by the arrow.

$$V_{bi}^{(2)} = \frac{qn_{D,2}x_2^2}{2\varepsilon} \tag{4b}$$

The resulting band structure is shown in Fig. 2 (a) where $n_{D,1} < n_{D,2}$, and so the value of the conduction band in the RHS quasi-neutral region is lower by $\left|kT\ln\left(n_{D,1}/n_{D,2}\right)\right|$, and the built-in potential differ by the same value. The parameters used to construct this band structure or those of silicon, with a band gap of 1.12 eV, and $\varepsilon_r = 11.7$.

When V_A is set to a non-zero bias, the magnitude of the band bending on either side will change, and Eqs. 4 yield the band bending values $\Delta V^{(1)}$ and $\Delta V^{(2)}$, which is shown in Fig. 2 (b). In this band diagram, it is clear that the LHS depletion region is significantly shorter, causing a smaller band bending as expected in forward bias. The RHS is further depleted, and the band bending is larger.

C. Potential Distribution Across the Boundary.

Eqs. 1 and 3 fully describe the potential drop over the grain boundary without any approximations, and reveal asymmetry in the distribution of potential even for a symmetrically doped system. Keeping with the polarity of V_A described in Eq. 3, a positive bias will inject electrons into the left-hand side grain, reducing its depletion width and effectively inducing forward bias conditions, while the depletion region on the right-hand side expands as it enters a 'reverse' mode. The system, thus, can be viewed as two resistive components in series analogous to a voltage divider, where the majority of voltage drop occurs over the larger resistor, *i.e.*, the side of the boundary that is in reverse bias.

Nevertheless, since the total potential difference over the two components must amount to the applied value, the potential distribution can be described via a fraction, α, so that the potential drop on the LHS is $V^{(1)} = \alpha V_A$ and correspondingly, $V^{(2)} = (1-\alpha)V_A$ on the RHS, and α is

$$\alpha = \frac{V_{bi}^{(1)} - \Delta V^{(1)}(V_A)}{V_A} \tag{5}$$

And is schematically demonstrated in Fig. 2 (b).

Fig. 2 (c)-(e) show the values of α as a function of the RHS charge density for LHS densities of 0.8 (c), 1.0 (d) and 1.2×10^{16} cm^{-3} (e) and for external bias values ranging from $V_A = -0.5$ to $+0.5$ V. The value $\alpha = 0.5$ is indicated as a gray dashed line. In all the panels, the value of α increases with the RHS charge density and decreases with LHS values. This is justified through the balance of depletion widths, as the LHS depletion width is a proportional to the square root of the ratio of doping, $x_1 \propto (N_{D2}/N_{D1})^{1/2}$, as well as the total doping (See Supplementary Material for further details). When this ratio increases, *i.e.*, when the RHS is more conductive than the LHS, the potential distribution will skew to the LHS to compensate for the imbalance, and vice versa.

Fig. 2 (f) shows calculated α as a function of charge density on the RHS for different $n_{D,1}$ levels and values of externally applied bias, ranging between $V_A = -0.5$ (black traces), 0.005 (red traces), and 0.5 V (blue traces). Within each group, the effective doping of the LHS grain monotonously ranges between $n_{D,1} = 0.8$ at the top and 1.2×10^{16} cm^{-3} at the bottom, as indicated by the curved arrows. The decreasing values of α with increased V_A is consistent with the qualitatively discussed model of the junctions, where a larger applied bias renders a less resistive LHS component, which incurs a smaller fraction of the potential drop.

D. Transport Through Grain Boundaries.

The divergence of α from the expected value of 0.5 has significant implications for the proposed model, as the current is exponentially dependent on α. In developing the current equation for a grain boundary, we consider the case of a wide depletion region, through which the dominant conduction mechanism is thermionic emission[27,28]. For brevity, the main considerations in developing the model are presented before discussing the resulting current equation. The full derivation can be found in the Supplementary Material. Following the reasoning presented by Schottky in the derivation of the metal-semiconductor current equation, the current from each side of the interface is considered separately. The current from the LHS is given by:

$$I_{1\to 2} = A \int_{F_{N,1}+\phi_{B,1}}^{\infty} q v_x dn \tag{6}$$

Where A is the grain cross sectional area, v_x is the electron velocity in the positive x direction, and $dn = g_c(E) f_{FD}(E) dE$ is the density of electrons per energy within the conduction band, where $g_C(E)$ is the density of states in the conduction band, $f_{FD}(E)$ is the Fermi-Dirac distribution function and E is the energy.

The minimal electron velocity that allows it to traverse across the boundary is

$$\frac{1}{2} m_n^* v_{x,\min}^2 = q\left(V_{bi}^{(1)} - \alpha V_A\right) \tag{7}$$

Expressed in Eq. 6 through the lower integration limit, which is the height of the potential barrier taken from the electron quasi-Fermi reference level, $\phi_{B,1} = E_C - F_{N,1} + q(V_{bi}^{(1)} - \alpha V_A) \equiv \phi_{B,1}^{\circ} - q\alpha V_A$. The solution for Eq. 6 is

$$I_{1\to 2} = A\mathscr{A}^* T^2 \exp\left(-\frac{\phi_{B,1}^{\circ} - q\alpha V_A}{k_B T}\right) \tag{8}$$

Where $\mathscr{A}^*$ is the modified Richardson constant. Equivalently, the RHS current is

$$I_{2\to 1} = A\mathscr{A}^* T^2 \exp\left(-\frac{\phi_{B,2}^{\circ} - q(1-\alpha) V_A}{k_B T}\right) \tag{9}$$

And so, the net current is:

$$I = A\mathscr{A}^* T^2 \left[\exp\left(-\frac{\phi_{B,1}^{\circ} - q\alpha V_A}{k_B T}\right) - \exp\left(-\frac{\phi_{B,2}^{\circ} - q(1-\alpha) V_A}{k_B T}\right)\right] \tag{10}$$

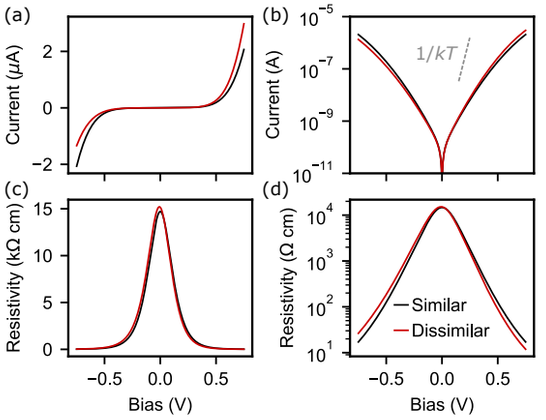

FIG. 3. (a)-(b) Current-voltage plots in linear (a) and semi-logarithmic (b) scales for 2G:1B systems with similar (black) and dissimilar (red) systems. (c)-(d) Resistivity-voltage plots in linear (c) and semi-logarithmic (d) scales for the same system.

Fig. 3 shows current-voltage and resistance-voltage plots for a symmetric 2G:1B system with $n_{D,1} = n_{D,2} = 10^{16}$ cm^{-3} (black curve) and for an asymmetric system, where the effective charge density levels, $n_{D,1} = 0.9 \times 10^{16}$ cm^{-3} and $n_{D,2} = 1.1 \times 10^{16}$ cm^{-3} (red curve), represent the extreme percentiles of the normal distribution, while maintaining an overall equal densities between the systems. For both curves, as the externally applied bias increases, the depletion region on the LHS grain becomes progressively narrow and the potential barrier decreases, as was demonstrated in Fig. 2 (b), whereas the RHS depletion extends and the current traversing from right to left becomes negligible, resulting in an exponentially increasing net current. However, it is important to note here that the slope of the current increase is smaller than the slope observed in an ideal Schottky junction. While for the latter, the potential drop is entirely on the semiconductor side of the junction, resulting in a semi-logarithmic slope of $(kT)^{-1}$ seen as a dashed gray line in Fig. 3 (b), the split of the applied potential in the 2G:1B system means that some of the potential is 'lost' on increasing the RHS depletion width, resulting in a lower semi-logarithmic slope of $S \sim (2.4kT)^{-1}$ for the symmetric system.

E. Asymmetry in Transport Properties of Dissimilar Grains.

While the transport properties of the symmetric and asymmetric systems are qualitatively similar, it is clear from Fig. 3 (a) that the current in the asymmetric system reaches a higher magnitude

at positive bias and lower (absolute) magnitude at negative bias. The asymmetry here is such that the RHS has higher doping, and so, in positive bias, when the RHS is driven into reverse conditions, smaller extension of the depletion width is required to balance the reduction on the LHS, and so a larger fraction of the bias is left to reduce the potential barrier on the LHS which determines the current. In negative bias conditions, the situation is reversed, where larger fraction of the bias is required to extend the depletion on the LHS, and the reduction in the RHS potential barrier is of a smaller magnitude. This is also manifested through the semi-logarithmic slopes of the system that are $|S| \sim (2.2\ kT)^{-1}$ and $\sim (2.5\ kT)^{-1}$, for positive and negative bias, respectively.

These observations are further emphasized by the resistivity traces shown in Fig. 3 (c) and (d), where the maximal resistivity for the asymmetric system is larger by 3.5%, despite having an overall equivalent density of carriers. Interestingly, the resistivity plot for the asymmetric system is skewed to the (lesser doped) LHS, resulting in a shift in the bias at which the maximal resistivity occurs, with the maximal (interpolated) resistivity for the symmetric system at $V_A = 0$ mV and for the asymmetric system at $V_A \approx -7.5$ mV. This behavior can be traced back to the split in potential drop, as manifested in α, when we consider the grain boundary resistivity as $\rho \propto (dI/dV_A)^{-1}$. The significant terms for positive and negative bias are shown in Eq.11.

$$\rho \propto \left[\frac{q\alpha}{kT}\exp\left(-\frac{\phi^{\circ}_{B,1} - q\alpha V_A}{kT}\right) - \frac{q(1-\alpha)}{kT}\exp\left(-\frac{\phi^{\circ}_{B,2} - q(1-\alpha)V_A}{kT}\right)\right]^{-1} \tag{11}$$

Keeping in mind that $\alpha_{\text{asym}} > \alpha_{\text{sym}}$ for all bias values in systems where $N^{(1)} < N^{(2)}$, it is clear that the resistivity is expected to be lower on positive bias that is governed by the first exponent term and vice versa (See Supplementary Material for further discussion).

III. NUMERICAL ANALYSIS

A. The 3G:2B System.

For the proposed model to be of practical value, it must be able to describe realistic materials where many grains are connected, in series and in parallel, to other grains via non-linear boundaries. However, extending the model to three grains and two boundaries (3G:2B) increases the number of degrees of freedom in the system to 5, namely, the depletion width on each side of each

boundary, and the fraction of the overall applied bias falling on each grain. For increased accuracy, the system must be described by 8 degrees of freedom, as the potential drop over the quasi-neutral grains cannot be neglected, or for a general case of (mG:($m-1$)B), a system is fully described by $4(m-1)$ degrees of freedom.

It is clear that such a set of equations can be formulated as a sparse matrix, if the model developed in the previous section can be codified, analytically or otherwise. Here, *LTSpice by Analog Devices*, which is in ubiquitous use and is free to use is utilized. To demonstrate the implications of random charge density across the system, a 3G:2B system is considered first. A detailed explanation to our approach for simulating this system follows, and larger more complex systems will largely follow the same methodology. The model system consists of 3 grains of equal size, $r_g = 300$ nm, for which the distribution of effective charge density has been discussed in Fig. 1. The level of complexity in evaluating Eqs. 1 and 3 in situ during the solution renders this approach as ineffective. Instead, look-up table (LUTs) are constructed for every combination of charge density levels which has a reasonable probability of being chosen. Since the grain charge densities will be randomly chosen from a Gaussian distribution of doping levels we must consider the very extreme cases of this distribution. In this case the extreme values were chosen to be $\mu_s \pm 1.5\times10^{15}$ cm^{-3}, for which the cumulative distribution is 2.9×10^{-7}, *i.e.*, less than one in every one-million grains.

The LUTs are built with charge density resolution of 5×10^{13} cm^{-3}, and with a constant surface charge density at the grain boundary of $n_T = 4\times10^{11}$ cm^{-2}, which satisfies the conditions stated in Sec. II B. Without loss of generality, dielectric and transport parameters matching those of polycrystalline silicon are used for the simulation. The external bias values range from -0.5 to $+0.5$ V, with a step resolution of 0.5 mV. It is important to note here that the voltage considered in building the LUTs is the local potential drop over the specific boundary; the overall applied voltage will be considered via the netlist in a later stage.

The LUTs are constructed iteratively, by solving Eqs. 1 and 3 with the relevant parameters. The overall potential drops on each side of the boundary, $\phi_{B,1} = \phi^{\circ}_{B,1} - q\alpha V_A$ and $\phi_{B,2} = \phi^{\circ}_{B,2} + q(1-\alpha)V_A$ are evaluated directly from the resulting depletion width, without the need to assess α explicitly. The current is calculated from Eq. 10 and subsequently, the resistance of the boundary is assessed from $R_B = V_A/I$. The LUTs store both the depletion width and the resistance as a function of the applied bias.

When the library of LUTs is complete, a netlist can be generated. A general schematic of

the netlist represented as a circuit diagrams is shown in Fig. 4 (a). Self-consistent treatment of the model dictates that the expansion and contraction of the depletion region will affect the resistance of the quasi-neutral regions of the grains as well as the boundaries. Hence, each grain is represented as two resistors, with the resistance of each determined by its adjacent boundary. For example, if the depletion width, x_1 of a boundary expands by $\delta x = x_1(V_A) - x_1(0)$, the resistance of its adjacent grain components is reduced by $\Delta R_G = -\rho_G \delta x / A$ where the resistivity is determined by $\rho_G = (q\mu_n n_D)^{-1}$.

Fig. 4 (b) shows the resistivity as a function of applied bias for 10^3 randomly sampled 3G:2B grains. The shape of each trace in Fig. 4 (b) is qualitatively similar to the single boundary trace shown in Fig. 3 (c), however, the spread of magnitudes shows that the small variations microscopic properties, *i.e.*, the individual grain charge density introduced through the sharp ($\sigma_s = 0.03\mu_s$) Gaussian distribution, results in a large variance in the macroscopic observables.

Fig. 4 (c) shows a histogram of the resistivities just over zero ($V_A = 0.5$ mV). The distribution is clearly skewed to higher values, which is in agreement with our previous observation (Fig. 3 (c)) that deviation from uniform charge density levels result in increased resistivity. To account for the arbitrary skewness observed, the distribution is fitted with a translated Weibull distribution, the probability distribution function (PDF) of which is shown by the solid red line in Fig. 4 (b). The translated Weibull PDF is given by:

$$f(x) = \frac{\beta}{\theta}\left(\frac{x-\delta}{\theta}\right)^{\beta-1} \exp\left(-\left(\frac{x-\delta}{\theta}\right)^{\beta}\right) \tag{12}$$

For $x \geq \delta$. Here β is the shape parameter, θ is the scale and δ is the shift parameters. The methodology used to estimate the three fitting parameters, as well as the extraction of parameters is discussed in the Supplementary Material.

The results of the 3G:2B sample are compared here with a uniformly doped 3G:2B, where $n_D = 1.00 \times 10^{16}$ cm^{-3} for all three grains. The Weibull mean estimated from this analysis is $\mu_W =$ 10.5 kΩ cm, which is a 7% increase over the uniform benchmark system where $\rho = 9.8$ kΩ cm. The standard deviation is $\sigma_W = 2.4$ kΩ cm, which amounts to $\sigma_W = 0.23\mu_W$.

B. Statistics of Larger Systems.

Interestingly, when assessed at any other voltage point across the resistance plot, the Weibull shape parameter, β remains the same with $\beta_W = 2.35 \pm 0.02$, suggesting that the distribution

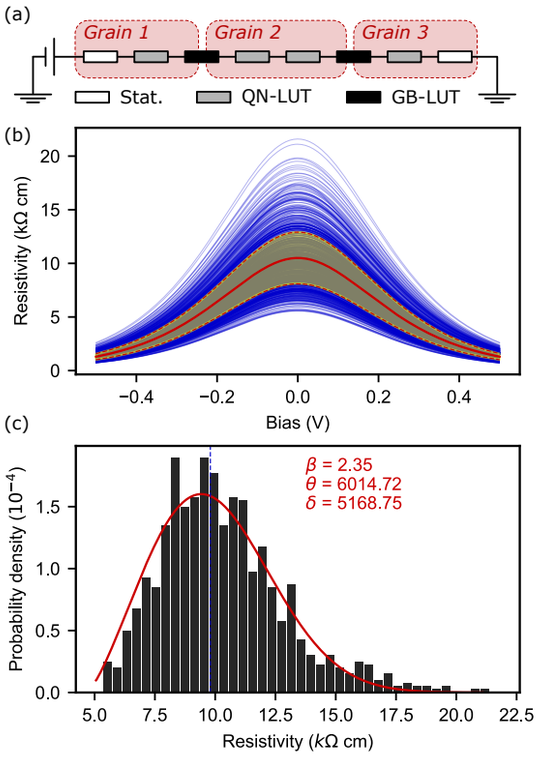

FIG. 4. (a) Schematics of the circuit diagram used to simulate a 3G:2B system, where white shaded resistors are static, gray shaded resistors are the quasi-neutral regions for which resistance is a function of the potential drop over the near grain boundary, and black are the grain boundary elements. (b) Resistivity-voltage traces of 10^3 simulations of the 3G:2B system (solid blue). The red line indicates the mean resistance, and the shaded yellow area indicates the part of the distribution within one standard deviation from the mean, bordered by the dashed red lines. (c) The distribution of resistivities just over zero bias. The solid red line indicates the probability density function of a fitted translated Weibull distribution, for which the parameters are noted on the panel. The dashed blue line indicates the expected resistivity of a uniformly distributed (10^{16} cm^{-3}) system.

describes inherent properties of the system that stem from its charge density variations, rather than effects that relate to the operating point displayed in the figure. Likewise, the normalized standard deviation remains $\sigma_W/\mu_W = 0.226 \pm 0.002$ across the whole voltage span. This is demonstrated visually by the solid red line which follows $\mu_W(V_A)$, and the area highlighted in yellow which follow $\mu_W(V_A) \pm \sigma_W(V_A)$.

Extending the one-dimensional chain system up to 10G:9B shows that the results largely follow a similar pattern with a few minor differences. First, the positive skew of the distribution slowly

vanishes, decreasing from $sk(\beta = 2.32) = 0.44$ for a 2G:1B system, seen in Fig. 5 (a), down to $sk(\beta = 3.33) = 0.07$ for 10G:9B, seen in Fig. 5 (b). The transition to a symmetric distribution is caused by the prevalence of chains with larger density fluctuations that have higher resistivity. This can be demonstrated by the distance of the mode of the distribution from the nominal resistivity of a uniform chain. For 2G:1B, the mode of the distribution is 7.44 kΩ cm which is 1.2% higher than the uniform chain. Here, the long tail to the right of the mean is generated by those chains that have large density variations. In contrast, for the 10G:9B chains, the mode is 14.3 kΩ cm which is 7.8% higher than the uniform chain. In this case, it is no longer a minority of chains that contribute higher resistivity values and the distribution is shifted to larger resistivities.

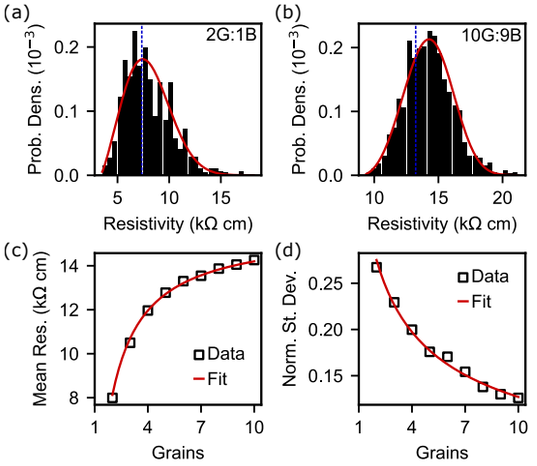

FIG. 5. (a)-(b) Probability densities for the resistivities of 2G:1B (a) and 10G:9B (b) systems. The solid red line is a fitted translated Weibull distribution, for which the parameters are discussed in the main text. The dashed blue line indicates the expected resistivity of a uniformly distributed (10^{16} cm^{-3}) system. (c) The mean resistivity of mG:(m-1)B chains. The solid red line is a fit to Eq. 13 discussed in the main text. (d) The normalized standard deviation for the systems described in (c). The solid red line is the fit to $m^{-1/2}$.

An increase in resistivity with growing chains is detailed in Fig. 5 (c). The increase follows

$$\rho(m) = \frac{mL_g\rho_g + (m-1)L_b\rho_b}{mL_g + (m-1)L_b} \tag{13}$$

Shown by the red line and is attributed to the apparent increase in line-density of grain boundaries across the chain. The fitted parameters are $L_g = 670$ and $L_b = 52$ nm, and $\rho_g = 0.9$ and $\rho_b = 2.2 \times 10^5$ Ω cm. Critically, Eq. 13 saturates at very large m numbers to $\rho(\infty) = (L_g\rho_g + L_b\rho_b)/(L_g + L_b)$ which here has a value of 15.6 kΩ cm, an increase of 18% compared to

the uniformly doped material. Interestingly, a decrease in the normalized standard deviation occurs in conjunction to the increase in resistivity, and $\sigma(m)/\mu(m) \propto m^{-1/2}$, in agreement with the central limit theorem, suggesting that a reliable representation of the material as a bulk, emerges, where microscopic fluctuations balance out. This analysis demonstrates the significant advantage of representing a polycrystalline semiconductor through a distribution function, which is size dependent, as it fully describes the behavior of non-deterministic conductors and is able to hedge the uncertainty associated with them, which is usually perceived as a hindrance to incorporating these materials into functional devices.

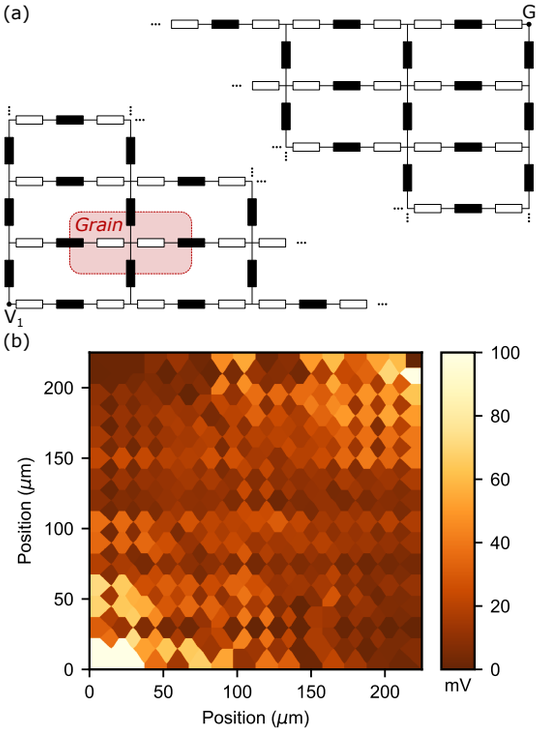

FIG. 6. (a) Part of a schematic diagram of the circuit used to generate the potential map shown in (b). A repeating unit (grain) is indicated on the figure. The excitation (V_1) and ground (G) points are noted. (b) A differential potential map of a 15×15 grains system. The colors represent potential drop over individual (grain / boundary) components.

Finally, the model is extended to a two dimensional film, measuring 15 by 15 grains, as shown schematically in Fig. 6 (a). Here, a single bias point, denoted by V_1 at the bottom left corner of the diagram, is sourcing the film with 15 V, and a single outlet, denoted by G at the top right corner, acts as a ground. The non-uniform cascade of potential caused by local variations of charge density

is seen in Fig. 6 (b), where each data point shows the potential drop over an individual circuit elements. The microscopic irregularities seen in the figure mean that the potential drop is not uniform, even in larger systems. This in turn means that charge transport through a polycrystalline film propagate in unique percolation paths, enabling the realisation of devices based on physical random values, such as encryption keys and position sensors.

IV. CONCLUSIONS

We developed a self-consistent model for electrostatics and transport across grain boundaries in polycrystalline films, where no a-priori knowledge of observable transport properties is required. The model yields a potential drop fraction, α which is instrumental for the accurate description of transport and was not considered in earlier works. The behavior of α in systems with different doping levels and under bias is explained through charge balance requirements within microscopic grains. The model is then extended to bulk using look-up tables-based circuit simulation, from which it is concluded that a statistical description of transport in non-deterministic materials is clearly associated with density of boundaries and charge density variations.

The comprehensive description of transport through a distribution function could prove to be an important tool in designing applications based on polycrystalline films, whether as means to understand macroscopic behaviors, such as in transparent conducting electrodes or polycrystalline TFTs, or for functionality based on microscopically random structures, such as in physical unclonable functions. The inclusion of capacitive behavior of the boundary will open new avenues for research in high-frequency response of polycrystalline semiconductor films.

SUPPLEMENTARY MATERIAL

See the Supplementary Materials for a detailed derivation of the electrostatics of grain boundaries and the resulting transport equations, a discussion of the Translated Weibull Distribution and methodology used for determining its parameters, and an example SPICE netlist of a 2G:1B system.

AUTHOR CONTRIBUTIONS

E.L.C. Benford: Software, formal analysis, methodology, data curation, writing. I. Amit: Conceptualization, methodology, validation, formal analysis, writing, supervision, funding acquisition.

CONFLICTS OF INTEREST

There are no conflicts to declare.

DATA AVAILABILITY

The data that support the findings of this study are openly available in GitHub at DOI:10.5281/zenodo.12800026

ACKNOWLEDGEMENTS

I. Amit is grateful for partial funding of this work by the Engineering and Physical Sciences Research Council (EPSRC) research grant number EP/Y002172/1.

REFERENCES

[1]J. Zhang, H. Yu, W. Chen, X. Tian, D. Liu, M. Cheng, G. Xie, W. Yang, R. Yang, X. Bai, *et al.*, "Scalable growth of high-quality polycrystalline mos2 monolayers on sio2 with tunable grain sizes," ACS Nano **8**, 6024–6030 (2014).

[2]R. A. Afre, N. Sharma, M. Sharon, and M. Sharon, "Transparent conducting oxide films for various applications: A review," Reviews on Advanced Materials Science **53**, 79–89 (2018).

[3]J. Kwon, M. Seol, J. Yoo, H. Ryu, D.-S. Ko, M.-H. Lee, E. K. Lee, M. S. Yoo, G.-H. Lee, H.-J. Shin, *et al.*, "200-mm-wafer-scale integration of polycrystalline molybdenum disulfide transistors," Nature Electronics , 1–9 (2024).

[4]W. G. Hawkins, "Polycrystalline-silicon device technology for large-area electronics," IEEE Transactions on Electron Devices **33**, 477–481 (1986).

[5]C.-H. Shen, P.-Y. Kuo, C.-C. Chung, S.-Y. Lee, and T.-S. Chao, "Stacked sidewall-damascene double-layer poly-si trigate fets with rta-improved crystallinity," IEEE Electron Device Letters **39**, 512–515 (2018).

[6]L. Zhang, J. Dong, and F. Ding, "Strategies, status, and challenges in wafer scale single crystalline two-dimensional materials synthesis," Chemical Reviews **121**, 6321–6372 (2021).

[7]J. Y. Seto, "The electrical properties of polycrystalline silicon films," Journal of Applied Physics **46**, 5247–5254 (1975).

[8]J. Martinez and J. Piqueras, "On the mobility of polycrystalline semiconductors," Solid-State Electronics **23**, 297–303 (1980).

[9]T. Kamins, "Hall mobility in chemically deposited polycrystalline silicon," Journal of Applied Physics **42**, 4357–4365 (1971).

[10]S. Christiansen, P. Lengsfeld, J. Krinke, M. Nerding, N. Nickel, and H. Strunk, "Nature of grain boundaries in laser crystallized polycrystalline silicon thin films," Journal of Applied Physics **89**, 5348–5354 (2001).

[11]I. Amit, D. Englander, D. Horvitz, Y. Sasson, and Y. Rosenwaks, "Density and energy distribution of interface states in the grain boundaries of polysilicon nanowire," Nano Letters **14**, 6190–6194 (2014).

[12]A. Shamir, I. Amit, D. Englander, D. Horvitz, and Y. Rosenwaks, "Potential barrier height at the grain boundaries of a poly-silicon nanowire," Nanotechnology **26**, 355201 (2015).

[13]F. Greuter and G. Blatter, "Electrical properties of grain boundaries in polycrystalline compound semiconductors," Semiconductor Science and Technology **5**, 111 (1990).

[14]H. Takeuchi, R. Yokogawa, K. Takahashi, K. Komori, T. Morimoto, Y. Yamashita, N. Sawamoto, and A. Ogura, "Thermal conductivity characteristics in polycrystalline silicon with different average sizes of grain and nanostructures in the grains by uv raman spectroscopy," Japanese Journal of Applied Physics **59**, 075501 (2020).

[15]H.-S. Wong and Y. Taur, "Three-dimensional" atomistic" simulation of discrete random dopant distribution effects in sub-0.1/spl mu/m mosfet's," in *Proceedings of IEEE International Electron Devices Meeting* (IEEE, 1993) pp. 705–708.

[16]H. Tsuji, T. Kuzuoka, Y. Kishida, Y. Shimizu, M. Kirihara, Y. Kamakura, M. Morifuji, Y. Shimizu, S. Miyano, and K. Taniguchi, "Surface-potential-based drain current model for polycrystalline silicon thin-film transistors," Japanese journal of applied physics **47**, 7798 (2008).

[17]N. Gupta and B. Tyagi, "On the mobility, turn-on characteristics and activation energy of polycrystalline silicon thin-film transistors," Thin solid films **504**, 59–63 (2006).

[18]P.-J. Lin, Y.-Y. Chiu, F. Chen, and R. Shirota, "Simulation study of the instability induced by the variation of grain boundary width and trap density in gate-all-around polysilicon transistor," IEEE Transactions on Electron Devices **68**, 1969–1974 (2021).

[19]Y. Zhou, M. Wang, D. Zhou, D. Zhang, and M. Wong, "An analytical expression for threshold voltage of polycrystalline-silicon thin-film transistors," IEEE Electron Device Letters **31**, 815–817 (2010).

[20]I. Steinke and P. Ruden, "Percolation model for the threshold voltage of field-effect transistors with nanocrystalline channels," Journal of Applied Physics **111** (2012).

[21]P. Suresh, K. Ramkumar, and M. Satyam, "Capacitance-voltage characteristics of grain boundaries in cast polycrystalline silicon," Journal of Applied Physics **69**, 8217–8221 (1991).

[22]N. J. McCullen, D. P. Almond, C. J. Budd, and G. W. Hunt, "The robustness of the emergent scaling property of random rc network models of complex materials," Journal of Physics D: Applied Physics **42**, 064001 (2009).

[23]O. Birkholz, Y. Gan, and M. Kamlah, "Modeling the effective conductivity of the solid and the pore phase in granular materials using resistor networks," Powder Technology **351**, 54–65 (2019).

[24]G. Ekanayake, T. Quinn, and H. Reehal, "Large-grained poly-silicon thin films by aluminium-induced crystallisation of microcrystalline silicon," Journal of Crystal Growth **293**, 351–358 (2006).

[25]A. Abass, D. Van Gestel, K. Van Wichelen, B. Maes, and M. Burgelman, "On the diffusion length and grain size homogeneity requirements for efficient thin-film polycrystalline silicon solar cells," Journal of Physics D: Applied Physics **46**, 045105 (2012).

[26]M. K. Hatalis and D. W. Greve, "Large grain polycrystalline silicon by low-temperature annealing of low-pressure chemical vapor deposited amorphous silicon films," Journal of Applied Physics **63**, 2260–2266 (1988).

[27]D. Joshi and R. Srivastava, "Mobility and carrier concentration in polycrystalline silicon," Solar Cells **12**, 337–344 (1984).

[28]J. Andrews, "Electrical conduction in implanted polycrystalline silicon," Journal of Electronic Materials **8**, 227–247 (1979).